

THE SSS PHASE OF RSOPHIUCHI OBSERVED WITH *Chandra* AND *XMM-Newton* I.
DATA AND PRELIMINARY MODELING

J.-U. NESS¹, S. STARRFIELD¹, A.P. BEARDMORE², M.F. BODE³, J.J. DRAKE⁴, A. EVANS⁵, R.D. GEHRZ⁶, M.R. GOAD², R. GONZALEZ-RIESTRA⁷, P. HAUSCHILDT⁸, J. KRAUTTER⁹, T.J. O'BRIEN¹⁰, J.P. OSBORNE², K.L. PAGE², R.A. SCHÖNRICH¹¹, C.E. WOODWARD⁶

Draft version October 22, 2018

ABSTRACT

The phase of Super-Soft-Source (SSS) emission of the sixth recorded outburst of the recurrent nova RS Oph was observed twice with *Chandra* and once with *XMM-Newton*. The observations were taken on days 39.7 (*Chandra*), 54.0 (*XMM-Newton*), and 66.9 (*Chandra*) after outburst. We confirm a ~ 35 -sec period on day 54.0 and found that it originates from the SSS emission and not from the shock. We discuss the bound-free absorption by neutral elements in the line of sight, resonance absorption lines plus self-absorbed emission line components, collisionally excited emission lines from the shock, He-like intersystem lines, and spectral changes during an episode of high-amplitude variability. We find a decrease of the oxygen K-shell absorption edge that can be explained by photoionization of oxygen. The absorption component has average velocities of $-1286 \pm 267 \text{ km s}^{-1}$ on day 39.7 and of $-771 \pm 65 \text{ km s}^{-1}$ on day 66.9. The wavelengths of the emission line components are consistent with their rest wavelengths as confirmed by measurements of non-self absorbed He-like intersystem lines. We have evidence that these lines originate from the shock rather than the outer layers of the outflow and may be photoexcited in addition to collisional excitations. We found collisionally excited emission lines that are fading at wavelengths shorter than 15 \AA that originate from the radiatively cooling shock. On day 39.5 we find a systematic blue shift of $-526 \pm 114 \text{ km s}^{-1}$ from these lines. We found anomalous He-like f/i ratios which indicates either high densities or significant UV radiation near the plasma where the emission lines are formed. During the phase of strong variability the spectral hardness light curve overlies the total light curve when shifted by 1000 sec. This can be explained by photoionization of neutral oxygen in the line of sight if the densities of order $10^{10} - 10^{11} \text{ cm}^{-3}$.

Subject headings: stars: novae, stars: individual (RS Oph) — X-rays: stars

1. INTRODUCTION

RS Oph is a Symbiotic Recurrent Nova (RN) that had recorded outbursts in 1898, 1933, 1958, 1967, 1985, and 2006 (February 12.83 = day 0; Hirosawa et al. 2006). In previous outbursts RS Oph was well-studied in the optical, and in 1985 it was followed extensively in ultraviolet (Shore et al. 1996, and references therein), radio (Padin et al. 1985; Hjellming et al. 1986), and X-rays (six pointings by *EXOSAT* from day 55 to day 251 of the outburst, Mason et al. 1987; O'Brien et al. 1992).

¹ School of Earth and Space Exploration, Arizona State University, Tempe, AZ 85287-1404, USA: [Jan-Uwe.Ness, summer.starrfield]@asu.edu

² Department of Physics & Astronomy, University of Leicester, Leicester, LE1 7RH, UK

³ Astrophysics Research Institute, Liverpool John Moores University, Birkenhead, CH41 1LD, UK

⁴ Harvard-Smithsonian Center for Astrophysics, 60 Garden Street, Cambridge, MA 02138, USA

⁵ Astrophysics Group, Keele University, Keele, Staffordshire, ST5 5BG, UK

⁶ Department of Astronomy, School of Physics & Astronomy, 116 Church Street S.E., University of Minnesota, Minneapolis, MN 55455, USA

⁷ XMM Science Operations Centre, ESAC, P.O. Box 50727, 28080 Madrid, Spain

⁸ Hamburger Sternwarte, Gojenbergsweg 112, 21029 Hamburg, Germany

⁹ Landessternwarte Königstuhl, 69117 Heidelberg, Germany

¹⁰ Jodrell Bank Observatory, School of Physics & Astronomy, University of Manchester, Macclesfield, SK11 9DL, UK

¹¹ Universitäts-Sternwarte der Ludwig-Maximilians-Universität, Scheinerstr. 1, 81679 München, Germany

RS Oph is a member of a small class of Cataclysmic Variables (CVs) in which a white dwarf (WD) orbits a red giant secondary (M2III). The orbital period is 455.72 ± 0.83 days and, assuming a WD near the Chandrasekhar Limit and a low inclination ($i < 40^\circ$), the red giant mass is of order $0.5 M_\odot$ (Dobrzycka & Kenyon 1994). The distance to RS Oph has been well determined by a variety of methods as $1.6 \pm 0.3 \text{ kpc}$ (Bode 1987). The interstellar absorbing column, $N_{\text{H}} = (2.4 \pm 0.6) \times 10^{21} \text{ cm}^{-2}$, was determined from H I 21 cm measurements (Hjellming et al. 1986) and is consistent with the visual extinction ($E(B-V) = 0.73 \pm 0.1$) determined from IUE observations in 1985 (Snijders 1987).

Just as in Classical Novae (CNe[†]), accretion of material from the secondary causes an explosion on the WD surface. However, in RNe the rate of mass accretion and the WD mass are sufficiently large for outbursts to repeat on human timescales. (The other members of this class are T CrB, V745 Sco, and V3890 Sgr).

A RN evolves analogously to a CN, the major difference between the two types of outburst arises from the presence of the red giant in the binary system which completely changes the environment around the WD. The evolution of the X-rays in RS Oph can be characterized by four phases:

- The explosion ejects material into its surround-

[†] The companion of the WD is generally a main-sequence star instead of a giant.

ings and produces a strong shock moving into the wind and outer atmosphere of the red giant and backwards into the ejecta (e.g., Bode et al. 2006; O’Brien et al. 2006; Sokoloski et al. 2006). The strength of the shock depends on the kinetic energy of the ejecta and the density of the medium into which the ejecta run.

- While nuclear burning continues on the WD, the bolometric luminosity is approximately constant (Gallagher & Code 1974). Depending on the opacity due to electron scattering within the expanding shell, the peak of the observed spectrum gradually shifts from low energies (optical and UV) to soft X-rays (Gallagher & Code 1974). In CNe this happens after a few weeks to months (e.g., V4743 Sgr; Ness et al. 2003b), and the spectrum resembles that of the class of Super Soft X-ray Binary Sources (SSS Kahabka & van den Heuvel 1997). This phase is therefore called the SSS phase.
- After the end of nuclear burning on the WD, the SSS emission decreases and RS Oph enters a phase in which a recombining plasma, exhibiting emission lines from radiatively excited states, appears.
- The final stage is that of the ejected material radiatively cooling. Collisional bound-bound excitations are balanced by radiative de-excitations, giving rise to emission lines (also called the coronal approximation). In this way kinetic energy is effectively converted into radiation.

The first few weeks of the evolution of the X-ray emitting blast wave in RS Oph were studied by Sokoloski et al. (2006) using the Rossi X-ray Timing Explorer (RXTE) and Bode et al. (2006) using *Swift*. The shock wave was also extensively studied at radio wavelengths by Very Long Baseline Interferometry (VLBI) and MERLIN imaging observations (O’Brien et al. 2006). From these observations, those obtained with the Hubble Space Telescope (Bode et al. 2007) and with ground-based infrared interferometers (VLTI+AMBER Chesneau et al. 2007), asymmetries and multiple emission components have clearly been established that show that there is jet-like ejection in addition to shell-like ejection of material. In the 2006 outburst *Chandra* obtained one, and *XMM-Newton* obtained two observations of this phase (Ness et al. 2006a; Drake et al. 2006; Gonzalez-Riestra et al. 2006, Ness in prep.).

The SSS phase commenced about 30 days into the outburst (Osborne et al. 2006c). Early in the evolution, the energy output of a nova explosion happens primarily at optical and UV wavelengths, because the high-energy radiation produced by nuclear burning on the surface of the WD will be scattered within the surrounding shell, leaving the atmosphere as lower-energy radiation. When the surrounding shell becomes thinner as a consequence of the expansion, the optical brightness decreases while the X-ray brightness increases and originates from deeper within the outflow. X-ray observations during this phase allow studies of the plasma regions at the radial distance from the WD within the outflow where the optical depth $\tau \approx 1$. The spectrum is a hot stellar atmosphere whose

peak energy and shape are dominated by the temperature and by interstellar and circumstellar absorption. In CNe, additional absorption lines have been observed (e.g., V4743 Sgr, Ness et al. 2003b) which originate from highly ionized species and are shifted and broadened according to the dynamics of the observed plasma.

X-ray observations of the 1985 outburst taken with *EXOSAT* after day 55 (Mason et al. 1987) were modeled by O’Brien et al. (1992) assuming the emission to originate from the shocked wind. A direct comparison of the shapes of the light curves taken with *EXOSAT* and with *Swift* in 2006 (Osborne et al. 2007) show a remarkable resemblance, implying that the spectra obtained in 1985 (at least in the case of the LE of *EXOSAT*) were actually dominated by the SSS emission (Ness et al. 2007).

We present three grating observations taken during the SSS phase. Two observations were taken with *Chandra* (Ness et al. 2006b) and one with *XMM-Newton*. We describe our method of extraction of the X-ray light curves and X-ray spectra in Sects. 2.1 and 2.2, respectively. We present our spectral analysis in Sect. 3, focusing on the broad-band continuum spectrum in Sect. 3.1, the resonance absorption- and emission lines in Sect. 3.2, emission lines originating from the shock in Sect. 3.3, He-like intersystem lines in Sect. 3.4, and the spectral changes during brightness variations detected during the first observation in Sect. 3.5. We discuss various possible interpretations in Sect. 4 and summarize our conclusions in Sect. 5.

2. OBSERVATIONS

TABLE 1
GRATING OBSERVATIONS DURING SSS PHASE

2006 Date start–stop	day ^[a]	Mission	Grating /detector	ObsID	exp. time (net)
March 24, 12:25:22	39.69	<i>Chandra</i>	LETGS	7296	10.0 ksec
–March 24, 15:38:20	39.82		/HRC		
April 07, 21:04:52	54.05	<i>XMM</i>	RGS1	0410180301	9.8 ksec
–April 08, 02:20:04	54.27		RGS2		18.6 ksec
April 20, 17:23:48	66.89	<i>Chandra</i>	LETGS	7297	6.5 ksec
–April 20, 20:27:57	67.02		/HRC		

^[a]after outburst (2006 Feb 12.83UT)

During the SSS phase that started after day 26 (2006 March 10), three grating observations were carried out by *Chandra* (Weisskopf et al. 2002) and *XMM-Newton* (Jansen et al. 2001). We summarize the dates of each observation, the respective days after the outburst, instrumental setup, observation identification numbers (ObsID), and the net exposure times in Table 1. The first and the last observations were taken by *Chandra* with net exposure times of 10.0 ksec and 6.5 ksec, respectively. As a consequence of the brightness of the source, telemetry saturation (full buffer all the time) occurred, which reduced the effective exposure times compared to the on-source times. Provisions were taken to ensure that these reduced spectra were correctly calibrated. We used the LETGS/HRC combination (Low Energy Transmission Grating/High Resolution Camera: Brinkman et al. 2000; Murray et al. 2000), which is an imaging disper-

sion spectrometer. Higher dispersion orders are not filtered out, but in our case contamination of the first-order spectrum by higher-order photons is negligible because the SSS spectrum is sufficiently narrow as to prevent an overlap of the dispersion orders.

The second grating observation during the SSS phase was taken with *XMM-Newton* (XMM) on day 54 after outburst (2006 April 7). XMM carries five X-ray instruments, three low-resolution CCD detectors and two gratings (Reflection Grating Spectrometers RGS1 and RGS2; den Herder et al. 2001). Due to the unexpected brightness of the target, the allocated telemetry rates were not sufficient to handle the large event rate. All instruments were affected by telemetry saturation. This implies that the effective exposure times were shorter than the on-target times. For the RGS2, the net exposure time was 18.6 ksec but only 9.8 ksec in the RGS1 (total on-target time was 18.9 ksec). Since the telemetry losses do not depend on the energy of the photons, they have no effect on the extracted spectrum, except for the shorter net exposure time. However, the light curves were strongly affected, since telemetry losses cannot be recovered. The X-rays dispersed into the spectrum by reflecting off the RGS are recorded with a strip of CCD detectors, and the wavelength range is 5–38 Å. Unfortunately, two chips within these CCD arrays failed early in the mission, and those portions of the dispersed spectrum that should be recorded by these chips are lost. The wavelengths affected by the chip failure range from 10.5–13.8 Å in the RGS1 and 20–24 Å in the RGS2. Since the peak emission of our SSS spectrum ranges between 15 Å and ~ 30 Å (see Sect. 2.2 and Fig. 3), only the RGS1 gives us sufficient spectral information, and we concentrate primarily on the RGS1 for spectroscopy. We use the RGS2 for light curve analyses. Since the source spectrum has its peak in the middle of the RGS2 chip gap (Fig. 3), the RGS2 collects fewer photons and is less affected by telemetry losses. This may be the only example where the chip gap is actually of use, providing us with the only useful light curve of this observation.

We present our extraction of the light curves in Sect. 2.1 and that of the spectra in Sect. 2.2. We used standard tools provided by the mission-specific software packages SAS (Science Analsis Software, version 7.0) and CIAO (Chandra Interactive Analysis of Observations, version 3.3.0.1).

2.1. Extraction and analysis of light curves

Chandra: For the extraction of *Chandra* light curves we used the CIAO tool `lightcurve`, which extracts all photons within previously defined source and background extraction regions on the detector. As source extraction regions we chose two polygons around the streaks of dispersed photons including both dispersion directions and we used only the middle chip (i.e., $\lambda < 50$ Å). The background was extracted from adjacent regions and subtracted.

XMM-Newton: For the extraction of *XMM-Newton* RGS2 light curve we used the SAS tool `evselect`, which extracts all dispersed photons within standard source- and background extraction regions. We extracted the RGS2 light curve in four different bin sizes in time, all chosen to be multiples of the readout time (4.5947 sec)

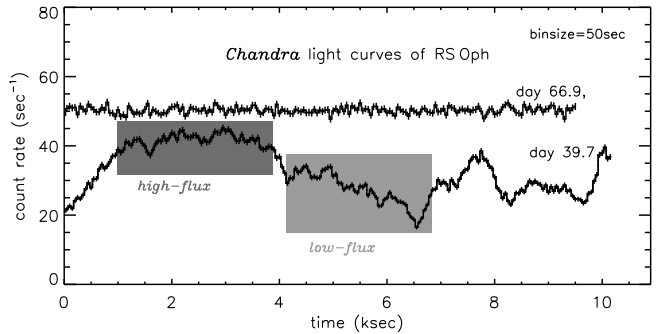


FIG. 1.— Light curves of the *Chandra* LETG observations, days 39.6 and 66.9, in time bins of 50 sec. The light curves have been extracted from the dispersed photons covering a wavelength range $\sim 6 - 50$ Å. For the first observation we extracted separate spectra from the time intervals marked with different shadings (see Fig. 9).

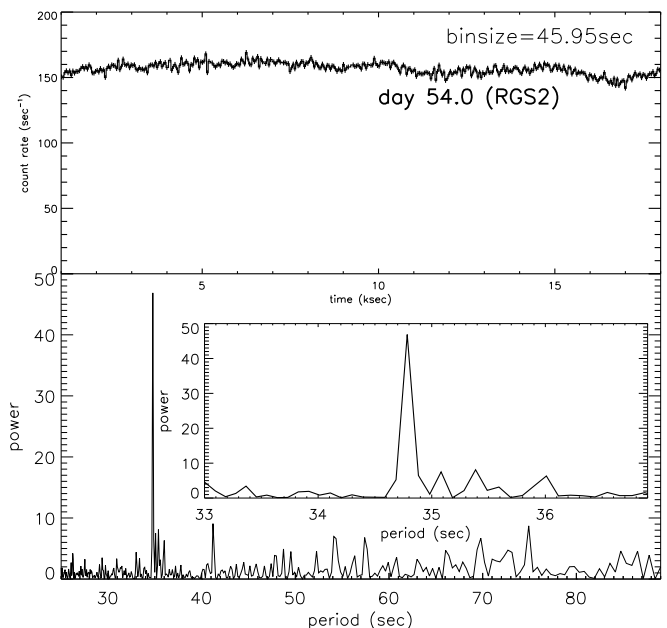


FIG. 2.— RGS2 light curve (day 54.0) in 45.947-sec time bins (10 times readout time, top) and periodogram (bottom). A ~ 35 -sec periodicity is found in the RGS2 light curve that confirms observations of a similar period with *Swift* reported by Osborne et al. (2006c).

in order to search for periodicity.

In Fig. 1 we show the *Chandra* light curves in 50-sec time bins in units of ksec after the start of each observation. In the observation of day 39.7, the count rate increases rapidly by a factor of two within only 1000 seconds, remaining at a high count rate for about 3000 seconds, then dips down (a little bit lower than the start count rate), only to rise again with an even steeper slope towards the end of the observation. In Fig. 2 we show the RGS2 light curve extract for day 54.0, which is much flatter than that on day 39.7, but is not as flat as on day 66.9. For the latter light curve we investigated the possibility of rapid variability, however, a simple model assuming a constant emission level reproduces the measured light curve with a reduced $\chi^2 = 0.94$, thus models including any kind of variability cannot improve the fit by more than 68.3%.

We computed a power spectrum for all light curves, and for days 39.7 and 66.9 we find no significant pe-

riodic variations. In order to search for periods shorter than 50 sec, we also extracted the *Chandra* light curves in smaller time bins, but did not detect any periods longer than 2 sec. In the bottom panel of Fig. 2 we show the result from the period search of the RGS2 light curve. In this observation we find a 34.8-sec period that is consistent with the ~ 35 -sec period reported by Osborne et al. (2006c). We also found a period of ~ 5.3 sec, which is the beat period of the instrument readout time (4.5947 sec) and the 34.8-sec period. We extracted the light curves from each chip and found this period only on those chips that recorded the SSS spectrum.

Our re-analysis of the *Swift* light curves obtained on days ≈ 39.7 , 54.0, and 66.9 indicated that the ~ 35 sec periodicity is only present on day 54.0. Osborne et al. (2006b) reported that this periodic variability was not always present, disappearing entirely after day 63 (2006, April 17).

We compared the emission levels in the grating spectra with those of *Swift* at the same times. The first observation was taken during the phase of highly variable soft X-ray flux reported in Osborne et al. (2006a,c). This phase lasted from days 29 to 46 (Osborne et al. 2006b) and is thus coincident with the highly variable light curve taken with *Chandra* on day 39.7. Since *Swift* light curves are never continuous over more than at most 2 ksec due to its orbit, it is the *Chandra* light curve that demonstrates that the source was actually variable on time scales shorter than 0.1 days.

Close inspection of the *Swift* monitoring light curve (Osborne et al. 2007) revealed that the first *Chandra* observation (day 39.7) was taken at a time when the *Swift* count rate was close to one of the minima during the variability phase, while the second *Chandra* observation (day 66.9) was taken during the decline shortly after the peak emission level had been reached. This explains the higher *Chandra* count rate on day 66.9 compared to day 39.7. The *XMM-Newton* observation was carried out during a phase of higher emission. We compared the relative emission levels between days 39.7, 54.0 and 66.7 by computing the photon fluxes by integration of the grating spectra (see Sect. 2.2). Within the uncertainties of the flux variations on day 39.7, the changes are consistent with the changes of the corresponding *Swift* count rates.

2.2. Extraction of spectra

Grating spectra are extracted on an equidistant wavelength grid (in units of \AA), and we use wavelength units throughout this paper. We extracted the spectra with the *Chandra* CIAO tool `tgextract` for the LETGS observations and the *XMM* SAS tool `rgsproc` for the RGS observation. These routines place standardized extraction regions over the dispersed photons on the detector and are optimized to maximize the ratio of collected source counts to the included background. The mirror point spread function is translated into an instrumental line profile that is approximately Lorentzian for the RGS and more Gaussian-like for *Chandra* LETG (both $\text{FWHM} \sim 0.055 \text{\AA}$ at all wavelengths, corresponding to $500\text{--}1100 \text{ km s}^{-1}$ from 30\AA to 10\AA , respectively). Velocities below these values that contribute to line broadening are difficult to determine. However, velocities from line shifts can be determined accurately (see Table 2 in

Sect. 3.2). Using standard tools to calculate the effective areas (in cm^2) and then dividing a count rate by the effective area at the corresponding wavelength results in a photon flux that is sufficiently independent of the instrument (RGS vs. LETGS). Thus, the photon flux spectra from the RGS1 and the LETGS can be compared (see Fig. 3).

Chandra: The dispersed photons are recorded in two streaks in opposite directions from the zero-th order, delivering two independent spectra. We co-added these two spectra for best signal to noise. In addition, independent analyses of the spectra can be carried out for consistency checks. In Fig. 3 we present the two *Chandra* observations (light and dark shadings) along with the *XMM* observation (solid line).

XMM-Newton: RGS data were processed with the SAS task `rgsproc` in SASv7.0 up to the creation of the merged, filtered event file. This file was manipulated to correct for pileup. Given the high flux of the source, spectra were extracted from the full field of view instead of using standard extraction regions, and no background subtraction was applied. The separation of spectral orders was accomplished by using the energy resolution of the CCDs. Pileup occurs when two or more events arrive at the same (or neighboring) pixel during the same readout frame. These photons are registered as a single event with an energy that is the sum of the energies of the individual events. In our case, pileup results in events with CCD-measured energies $n \times E$ (where $n = 1, 2, 3, 4$) while the photons are dispersed according to their individual wavelengths. Due to this pile-up, counts occur in the energy-dispersion plane in regions normally associated with higher orders. There is no ambiguity between pile-up and higher order dispersion due to the narrow spectral range of the super-soft continuum spectrum. We were thus able to reconstruct the true spectrum before pile-up by adding those events in the energy-dispersion plane back into the first order spectrum that resulted from pile-up in the first-order spectrum. The rates of the new first-order spectra are about 30 percent higher than before this correction.

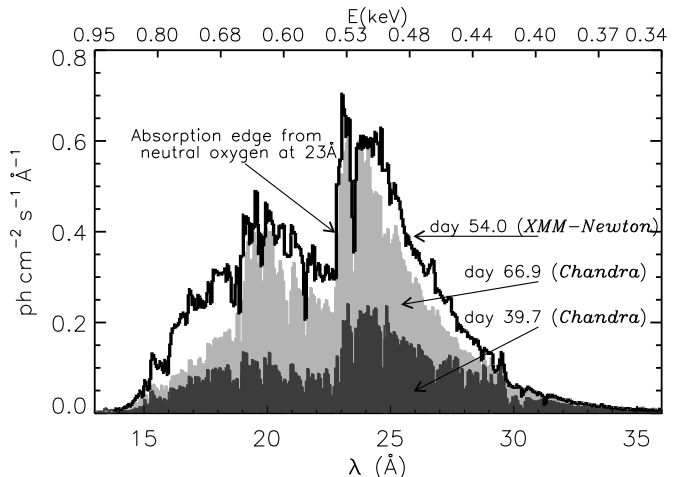


FIG. 3.— Comparison of all three grating spectra in units of photon fluxes obtained by dividing count rates by effective areas. The *Chandra* spectra are shown with shading and the RGS1 spectrum is a thick solid histogram line.

For a qualitative comparison of the spectra from the different missions we converted all three count rate spectra into photon flux spectra. We do not correct for the redistribution matrix, so the line profiles will still depend on the individual instrumental point spread function (PSF). However, the shape of the continuum is not affected by the instrumental PSF, as it is very small compared to the width of the continuum.

In Fig. 3 we compare the photon flux spectra of the three grating observations. The integrated fluxes relative to each other are consistent with the relative count rates *Swift* measured at the respective times. All spectra show continuum emission over the same wavelength range with similar shapes. At 22.83 Å there is a strong absorption edge in all spectra that is clearly non-instrumental and originates from O I (K-shell ionization). Also, an expected narrow $1s-2p$ absorption line at 23.5 Å (Paerels et al. 2001) from atomic oxygen can be identified in all three spectra. At ~ 29 Å there are emission line features in all spectra that we attribute to N VI (see Sect. 3.4). Strong absorption lines can be identified in all three spectra (see Sect. 3.2).

3. SPECTRAL ANALYSIS

3.1. Continuum emission and broad-band absorption

In order to understand the cause of the brightness changes we computed a series of blackbody models and found reasonable agreement with the measured spectra for temperature ranges $(630 - 830) \times 10^3$ K on day 39.7, $(650 - 710) \times 10^3$ K on day 54.0, and $(590 - 720) \times 10^3$ K on day 66.9. The bolometric luminosities, $\log(L_{\text{bol}})$, of these models are between 37.3 and 38.5 for day 39.7, 38.5 and 38.9 for day 54.0, and 38.2 and 39.3 for day 66.9. We used a standard model for interstellar plus circumstellar absorption. The value of hydrogen column density N_{H} was greater than the interstellar value ($N_{\text{H}} = 2.4 \times 10^{21} \text{ cm}^{-2}$) for all models (more below). However, the values of reduced χ^2 (χ_{red}^2) are greater than 20 for all models, and no secure conclusions can be drawn from these numbers. In particular, we don't claim from these models that Super-Eddington luminosities occurred. With these limitations we are not able to explain the brightness changes in terms of temperature or luminosity.

As a first approach to characterize the shape of the continuum, we computed hardness ratios $\text{HR} = (\text{H}-\text{S})/(\text{H}+\text{S})$ from the three spectra with H and S denoting the fluxes extracted from within the wavelength ranges 15–23 Å and 23–30 Å, respectively. We found values of -0.06, +0.12, and +0.03 with 4%, 1%, and 8% uncertainties for days 39.7, 54.04, and 66.9, respectively. Changes in hardness generally imply a change in temperature, but changes in broad-band absorption (bound-free transitions) by elements in the line of sight can also lead to changes in spectral hardness. We estimated the optical depth of the O I absorption edge at 22.83 Å from the intensities of the continuum, $\tau = \ln(\text{cont}_{\lambda < 22.8} / \text{cont}_{\lambda > 22.8})$, and found $\tau = 0.9$, 0.5, and 0.7 for days 39.7, 54.0, and 66.9, respectively. This implies that the larger hardness ratio on day 54 was caused by reduced O I within the material in the line of sight.

In order to investigate this effect closer, we use the blackbody models from above as continua and apply an absorption model that accounts for variations of the neu-

tral oxygen abundance. We optimized the blackbody parameters temperature and bolometric luminosity simultaneously with the parameters of the absorption model.

The continuum spectrum produced by the WD atmosphere has to pass through the circumstellar and the interstellar material in the line of sight. The former may be partially ionized while the latter consists of neutral elements of solar composition. The bound-free absorption imposed by this material leads to element-specific absorption edges that are detectable with the LETGS (e.g., Paerels et al. 2001). The depth of these edges depends on the elemental composition and absorption cross sections, e.g. for K-shell absorption by neutral oxygen. Absorption edges from higher ionization stages also depend on the fractional number density of the ion. We parameterize bound-free absorption in the line of sight by the column density of neutral hydrogen, N_{H} . While the column density of the interstellar material is assumed constant in all observations, it may vary with time in the circumstellar material. We, therefore, split the absorption into two terms, one term with fixed N_{H} and one with variable N_{H} , both with solar composition (Grevesse & Sauval 1998). We computed the total transmission coefficients as implemented in the software package PINTofALE (Kashyap & Drake 2000) from the single parameter N_{H} . Using this model we account only for absorption from the neutral component of the absorbing column while absorption by ionized elements is included only for helium.

In Fig. 4 we present the three spectra from the gratings (in photon flux units) in comparison with our best-fit continuum plus absorption models. First, we optimized the blackbody parameters and the value of N_{H} that represents the neutral component of the circumstellar material with the abundances fixed at solar (Grevesse & Sauval 1998). In the upper right corner of each panel we give the value of χ_{red}^2 . These models are identical to the ones described above, and are formally unacceptable. The blackbody continuum seems to represent the rough observed spectral shape. However, the high resolution of the gratings clearly exposes the shortcomings of blackbody models with many spectral features not being reproduced.

Next, we varied the abundance of the oxygen content within the circumstellar component, while the interstellar oxygen abundance remained fixed at solar. We fit the oxygen abundance simultaneously with the blackbody parameters and N_{H} and include the best-fit models with grey lines in Fig. 4. Although, these models are also formally unacceptable, an improvement in χ_{red}^2 is apparent. The resulting best-fit abundances suggest that after day 54 all neutral oxygen in the circumstellar material has disappeared. We note that for day 66.9 the optical depth around the edge was higher than on day 54.0, suggesting that the neutral oxygen abundance has increased again. The model for day 66.9 does not show this increase, but the peak is not well modeled. The blackbody temperatures of these models are $(540 - 760) \times 10^3$ K on day 39.7, $(520 - 580) \times 10^3$ K on day 54.0, and $(440 - 590) \times 10^3$ K on day 66.9. The bolometric luminosities, $\log(L_{\text{bol}})$, of these models are between 37.6 and 39.2 for day 39.7, 39.3 and 40.0 for day 54.0, and 38.9 and 40.5 for day 66.9. Comparison with the parameters of the models

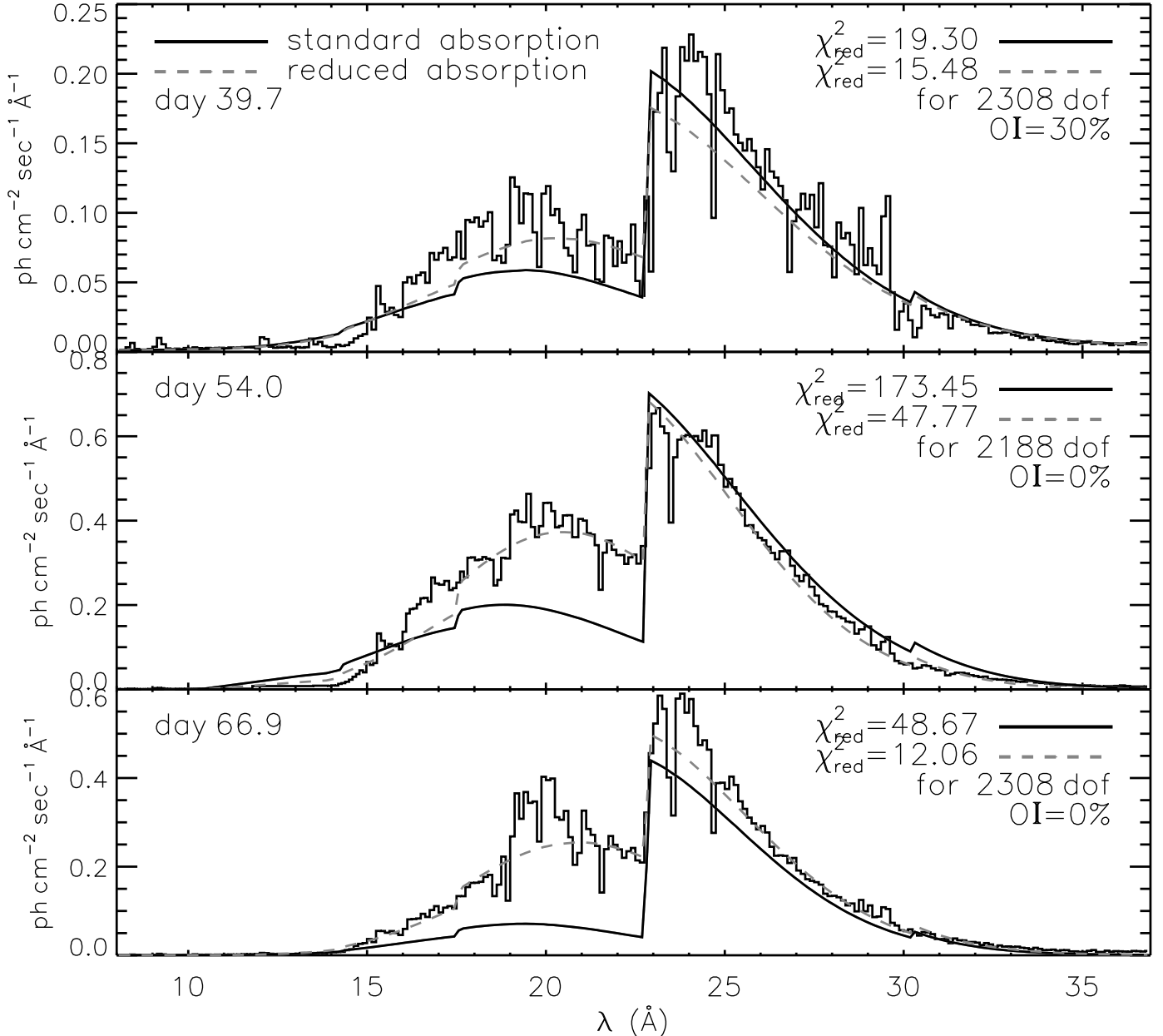


FIG. 4.— Three grating spectra of RS Oph in chronological order from top to bottom with a continuum model and two different absorption models applied to each case. The standard absorption models (black solid line) assume solar abundances for the neutral elements in the line of sight. For the second models (grey dashed) we allowed the abundance of neutral oxygen to vary. For all observations, both models have large χ^2_{red} , however, the assumption of reduced neutral oxygen leads to an improvement of the model.

with the oxygen abundance fixed at solar shows that the introduction of the oxygen abundance as a free parameter introduces considerable additional uncertainty in the blackbody parameters.

The simplest explanation for the reduction of neutral oxygen is photoionization of the circumstellar material by the radiation field. We tested this hypothesis and computed models with reductions of other elements that would also have to be ionized (nitrogen and carbon with their K-shell absorption edges at 30.25 Å and 43.63 Å, respectively). We were not able to find a model that reproduced the measured spectrum better than the one with only oxygen reduced. Next, we carefully inspected the grating spectra for evidence of any absorption edges at the ionization energies of O VII (16.77 Å),

O VIII (14.23 Å), N VI (22.46 Å), and N VII (18.59 Å). In all three spectra, there is no evidence for these absorption edges. Since the continuum level at these wavelengths is sufficiently high, and the instruments are sensitive enough to detect these edges, we conclude that no absorption edges from H-like and He-like ions are present. This indicates that the material that produces the absorption lines from high ionization stages (see next section) contributes little bound-free absorption and resides deeper within the outflow.

Paerels et al. (2001) pointed out that the detailed structure of the spectrum around the O edge is extremely complex, consisting of absorption lines and -edges for various ions and molecular species. For example, we studied the O I $1s - 2p$ absorption line at 23.62 Å. On days 39.7

and 66.9 we found this line at the same wavelength of 23.51 Å and with the same optical depth at line center of $\tau_c = 1.4$. This similarity suggests that this line was formed in a non-changing medium (interstellar medium). The shift of this line is similar to shifts 30-50 mÅ found by Juett et al. (2004) for various features from singly and doubly ionized oxygen in HETG spectra of seven X-ray binaries which are consistent with discrepancies between theoretical calculations and laboratory measurements. It is thus likely that the 23.51-Å line is the O I $1s - 2p$ line at the rest wavelength. We also found evidence for the $1s - 2p$ absorption lines of O II to O V, expected at 23.3 Å, 23.11 Å, 22.78 Å, and 22.33 Å, respectively (see also Table 3), which indicates that we are not only dealing with atomic oxygen.

Juett et al. (2004) have developed detailed models for the wavelength range around the oxygen K-shell absorption edge. These models allow determinations of the ratios of ionization stages and oxygen column densities and lead to a more accurate bound-free absorption model needed for further analyses. Similar analyses have been carried out by Page et al. (2003), however, in no other source is the oxygen edge as deep as in RS Oph.

Alternatively to ionization, Paerels et al. (2001) propose that grain formation could reduce the O edge. In the event of dust formation in the outer regions of RS Oph, oxygen could have been locked up in grains.

3.2. Modeling of resonance absorption and emission lines

The *Chandra* and *XMM-Newton* grating spectra are the only spectra that allow us to identify and study absorption- and emission lines. In Fig. 5 we show small portions of the *Chandra* count spectra of days 39.7 and 66.9, focused on the wavelength ranges of four prominent lines, projected on a velocity scale (assuming the rest wavelengths λ_0 given in the legends). We modeled these spectral regions with three components, a continuum (rescaled blackbody), an absorption line component, and an emission line component. We include the emission line component in order to determine if we are seeing P-Cygni profiles (Ness et al. 2006b). We restrict the model to the narrow spectral region around each line

$$M(\lambda) = \left\{ \left[C \times B_\lambda(T) + E \times G_e(\lambda, \lambda_e, \sigma_e) \right] \times \left[1 - A \times G_a(\lambda, \lambda_a, \sigma_a) \right] \right\} \times T_{\text{ISM}}(\lambda) \times T_{\text{CS}}(\lambda) \quad (1)$$

with $C \times B_\lambda(T)$ being the continuum (blackbody model) and $A \times G_a(\lambda, \lambda_a, \sigma_a)$ and $E \times G_e(\lambda, \lambda_e, \sigma_e)$ being the absorption- and emission line components, respectively, both modeled as Gaussians. In an iterative process we optimized the normalization C of the blackbody continuum at the fixed temperature $T = 6.2 \times 10^5$ K (based on the blackbody parameters found in Sect. 3.1) and the central wavelengths (λ_a and λ_e), line widths (σ_a and σ_e), and normalizations (A and E) of the absorption and emission line components, respectively. Finally, we corrected the model for interstellar and circumstellar absorption using the same absorption model described in Sect. 3.1 (without the reduction of neutral oxygen) with $T_{\text{ISM}}(\lambda)$ and $T_{\text{CS}}(\lambda)$ the transmission coefficients for interstellar and circumstellar material with $N_{\text{H}}(\text{ISM}) =$

$2.4 \times 10^{21} \text{ cm}^{-2}$ and $N_{\text{H}}(\text{CS}) = 2.3 \times 10^{21} \text{ cm}^{-2}$, respectively (equivalent to an effective HI column density of $4.7 \times 10^{21} \text{ cm}^{-2}$).

For a given transition with the rest wavelength λ_0 , the parameters λ_a and λ_e can be converted to velocities from line shifts (v_s) for the absorption- and emission line components, respectively. This velocity represents the expansion velocity at the radial distance within the outflow where the optical depth is unity. The line widths σ_a and σ_e are representative of the velocity distribution of the observed regions which depend on the velocity- and density profile within the outflow, however, we have not accounted for the contributions of the instrument profile and can therefore not use these numbers. We derive emission line fluxes from the parameter E and optical depths at line center, $\tau_c = \ln\{M(\lambda_{\text{min}})/\text{CONT}(\lambda_{\text{min}})\}$ at the wavelength where the model finds its minimum, λ_{min} . $\text{CONT}(\lambda_{\text{min}}) = C \times B(\lambda_{\text{min}}, T) \times T_{\text{ISM}}(\lambda_{\text{min}}) \times T_{\text{CS}}(\lambda_{\text{min}})$ is the continuum flux at λ_{min} . Note, that the emission line fluxes represent the intrinsic line fluxes, including self-absorption, corrected for interstellar plus circumstellar absorption. Integration over the entire absorption line profile allows us to estimate absorbing column densities, xn_e for each line. We use the oscillator strengths given in Table 2. The emission line fluxes and column densities depend strongly on the choice of $N_{\text{H}}(\text{ISM}) + N_{\text{H}}(\text{CS})$, especially at long wavelengths.

We calculated uncertainty ranges for the model parameters $\lambda_{a,e}$, $\sigma_{a,e}$, A , and E separately by calculating a grid of χ_{red}^2 over a given range of the respective parameters. For each grid point all other parameters were optimized, respecting the boundary condition of the individual parameter of interest to be fixed at the given grid value. The 1- σ uncertainty ranges were then obtained by interpolating the grid until χ_{red}^2 had increased by unity. If the curve was found to be too flat so that χ_{red}^2 never reached values higher than one above the minimum for a sensible range of values, then lower or upper limits were calculated. Next, the uncertainties of $\lambda_{a,e}$ and $\sigma_{a,e}$ were translated into the respective uncertainties in velocity, and those of A and E into the uncertainties of τ_c and emission line fluxes, respectively. For τ_c we only considered variations of A , but we allowed all other parameters to be optimized before a value of χ_{red}^2 was calculated for a given τ_c . The uncertainties of the column densities were obtained by calculating a grid of values of χ_{red}^2 from a range of pairs of A and σ_a that represent a grid of values of xn_0 and probing the range of $\chi_{\text{red}}^2 + 1$.

The uncertainties of τ_c and xn_0 do not explore the full uncertainty range as variations of the central wavelength of the emission line component can dramatically change those values. In particular if saturation is reached, we lose all constraints. This is a shortcoming of our parameterized model that cannot deal with saturation self-consistently. For now, the given uncertainty ranges represent the minimal uncertainties within which no changes can be considered significant. We have also not included uncertainties from the amount of interstellar and circumstellar absorption.

In Fig. 5 we compare the count spectra with the models $M(\lambda)$ after iteration of C , E , A , λ_e , σ_e , λ_a , and σ_a (Eq. 1). The relevant spectral ranges are well fitted, and the values of χ_{red}^2 are below 1.2 for day 39.7 and below 3.0

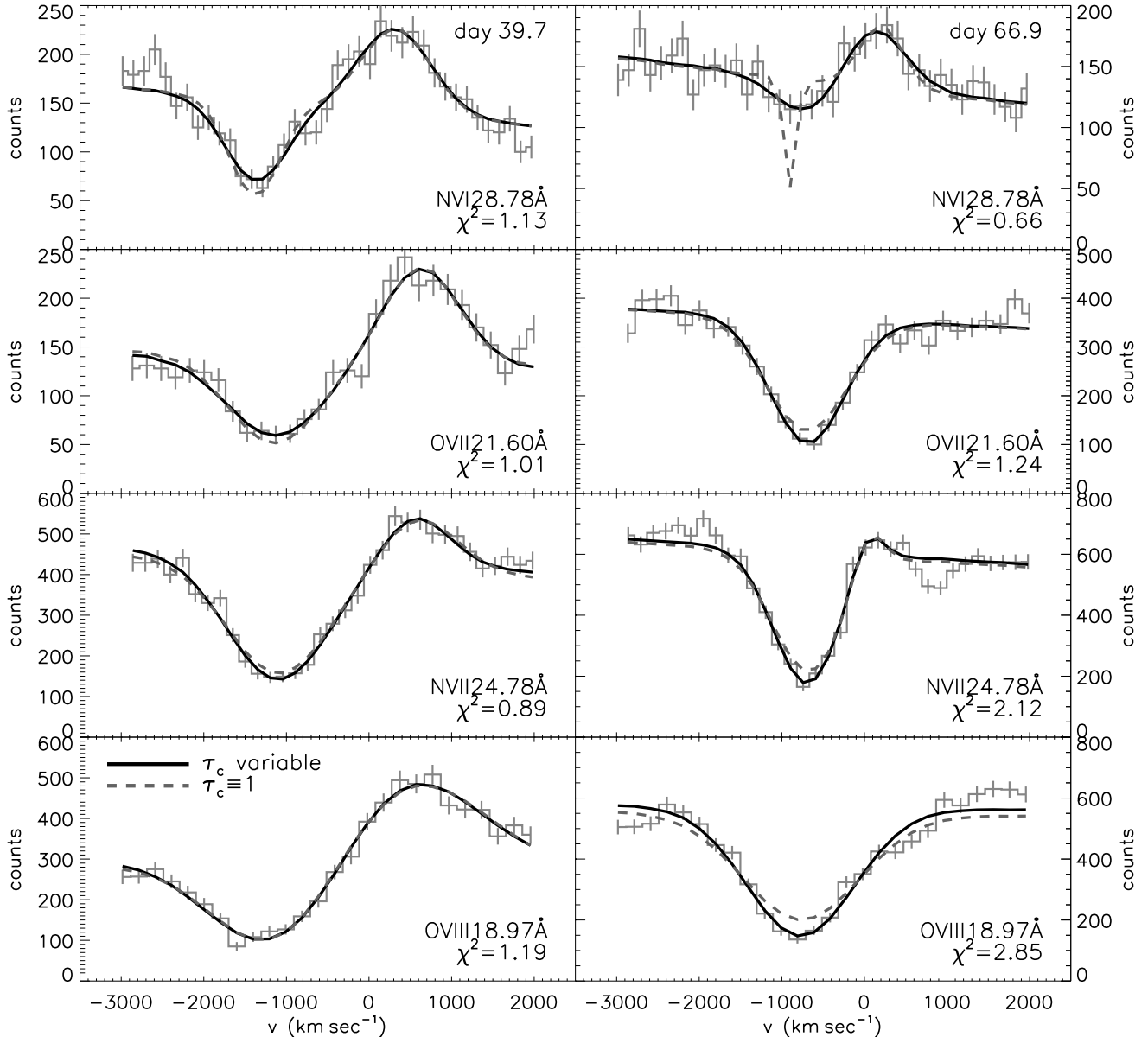


FIG. 5.— Modeling of resonance absorption- and emission lines detected on days 39.7 (left panels) and 66.9 (right panels) for four prominent transitions (labeled in bottom right). The models were calculated as described in Sect. 3.2 and the model parameters are shown in Table 2. The dashed lines mark models where the optical depth at line center, τ_c , was fixed at unity.

for day 66.9. In Table 2 we list the line-shift velocities, optical depths at line center, and emission line fluxes, derived from the model parameters with their uncertainty ranges for the absorption- and emission line components.

The optical depths in the line centers are unity within the uncertainties for all lines in both observations, which is consistent with our expectation that we are observing regions in the outflow where $\tau = 1$. In Fig. 5 we add a dashed lines denoting the respective models where $\tau = 1$ was enforced during the fit. For N VI (day 66.9) we were not able to constrain any of the parameters because the absorption trough is quite flat. An optical depth of $\tau = 1$ leads only to an acceptable fit if the absorption line is assumed to be very narrow and leads to an increase in χ^2 in only one spectral bin (see top right panel of Fig. 5).

The column densities could not be sufficiently constrained to assess whether they varied significantly from

day 39.7 to 66.9. Only N VII, and possibly N VI, exhibited a decrease of column density within the given errors. However, we caution that uncertainties from the emission line component and the continuum as well the amount of interstellar+circumstellar absorption are not included in these error estimates.

Within each observation the absorption line velocities are consistent with $-1286 \pm 267 \text{ km s}^{-1}$ for day 39.7 and $-771 \pm 65 \text{ km s}^{-1}$ for day 66.9 (weighted averages). This marks a clear reduction in the measured expansion velocity. The line widths, although dominated by the instrumental line profile, have systematically but not significantly decreased. We tested models where we fixed all line widths at the instrumental resolution ($\sigma_{\text{gauss}} = 0.03 \text{ \AA}$ at all wavelengths) and found acceptable fits except for N VII.

The potential of this approach over global approaches

is that we can concentrate on single lines that are least affected by blending or other uncertainties that are more difficult to disentangle in complex atmosphere models. We found optical depths at line centers of unity. The second reliable result at this stage is the decrease of the characteristic velocity consistently measured for five different absorption lines. Although the velocities derived from these absorption lines are very similar to those expected at these epochs from the simple shock model as applied to the Swift X-ray data (Bode et al. 2006), similar effects in these lines observed in X-rays in classical novae are commonly ascribed to observing material deeper into the envelope in which there is a velocity gradient (Hubble flow). Further, the origin of the emission line components has to be determined before further steps can be taken. This requires a reduction of the uncertainties which we plan to achieve by applying sensible boundary conditions.

For the observation taken on day 39.7, we first assumed only absorption lines, but an additional emission line component was necessary in order to arrive at acceptable fits. Their nominal (line-shift) velocities range from $\sim +300$ to $+600 \text{ km s}^{-1}$, but the uncertainty ranges are large and include the possibility that the emission lines could be at their rest wavelengths.

We scanned the *Chandra* spectrum of day 39.7 for all absorption lines that appear not to be blended and summarize the wavelengths and central optical depths τ_c below the continuum in Table 3. We attempted identifications and found lines from N, O, Fe, S, Si, Ca, and Ar using the collisional database APED[‡]. The identifications are based on the assumption that a strong collisional excitation probability implies a strong radiative excitation probability. We searched for candidates at wavelengths that imply blue shifts of $\sim 0.1 \text{ \AA}$, as this wavelength shift is found for the well-identified lines used for Fig. 5.

3.3. Emission lines from the shock

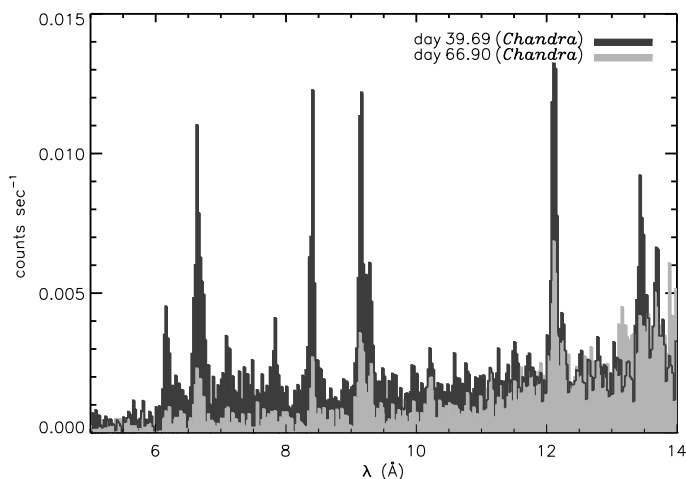


FIG. 6.— Comparison of the *Chandra* spectra taken on days 39.7 (dark) and 66.9 (light) focusing on the high-energy emission lines. These lines are independent of the SSS spectrum and are fading.

Shortwards of 14 \AA , we found emission lines at wave-

[‡] Astrophysical Plasma Emission Database v1.3 (Smith et al. 2001)

lengths where *Chandra* and *XMM-Newton* measured shock-induced emission lines before the SSS spectrum appeared (Ness et al. 2006a; Gonzalez-Riestra et al. 2006, Ness in prep.). In Fig. 6 we show the count rate spectra of this spectral range for the *Chandra* observations taken on days 39.7 and 66.9. In contrast to the SSS spectra on these days, the latter spectrum exhibits fainter emission lines than during the day-39.7 observation. These lines must be collisionally excited, due to the absence of any ionizing radiation of sufficient energies, and we interpret them as residual emission from the shock.

We measured wavelengths and emission line fluxes using our line fitting tool Cora (Ness & Wichmann 2002). The wavelengths can be converted to velocities that characterize the dynamics of the plasma that produces these lines. For day 39.7 we found a small systematic line shift from all lines that translate to a weighted average plus variance of $-526 \pm 114 \text{ km s}^{-1}$. For the other two observations, the lines were not strong enough to estimate reliable uncertainties of the line positions.

In Table 4 we list the emission line fluxes for the strongest lines. We have not corrected the measured fluxes for the effects of interstellar and/or circumstellar absorption. As shown in Sect. 3.1, our models of interstellar and circumstellar absorption are not accurate enough to derive reliable corrections. In the first four columns we list the line identifications, wavelengths, and transmission coefficients that would have to be applied under the assumptions of $N_{\text{H}}(\text{ISM}) + N_{\text{H}}(\text{CS}) = 4.7 \times 10^{21} \text{ cm}^{-2}$ and $N_{\text{H}}(\text{CS}) = 0$ (i.e., only interstellar absorption with $N_{\text{H}}(\text{ISM}) = 2.4 \times 10^{21} \text{ cm}^{-2}$) assuming solar abundances. As soon as a more accurate absorption model is available, the fluxes listed in Table 4 can be converted to unabsorbed fluxes at the source. However, if the lines originate from the shock, they may only be affected by interstellar absorption and not by circumstellar material. In the top part of Table 4 we list the line fluxes originating from the shock and in the bottom part we include the emission line fluxes measured as part of the models described in Sect. 3.2 for days 39.7, 54.0, and 66.9. We reference we label these lines 'hard lines' and 'soft lines', respectively. For the soft lines we reversed the correction for interstellar absorption that has been applied with the terms $T_{\text{ISM}}(\lambda) \times T_{\text{CS}}(\lambda)$ in Eq. 1 for comparison with the unabsorbed hard lines. We also include the line fluxes for He-like intersystem lines measured in Sect. 3.4. In the last three columns we list the changes in the line fluxes between days 54.0 and 39.9, 66.9 and 54.0, and 66.9 and 39.7, respectively.

The fluxes are all of the same order of magnitude which implies that they originate from the same plasma. In that case the soft lines considered as part of the absorption lines in Sect. 3.2 are actually coming from the shock. This would also explain why these lines disappeared by day 66.9, which earlier had been interpreted as disappearance of P Cygni profiles (Ness et al. 2006b). However, correcting for interstellar plus circumstellar absorption will result in considerable enhancements of the fluxes of the soft lines because of their longer wavelengths, but that depends critically on the value of $N_{\text{H}}(\text{ISM}) + N_{\text{H}}(\text{CS})$ and the applied absorption model. The resulting higher fluxes in the soft lines can be explained by photoexcitation in addition to collisional excitations. If the lines

TABLE 2
RESULTS FROM PROFILE FITTING ILLUSTRATED IN FIG. 5

ion	O VII		O VIII		N VI		N VII		Fe XVII	
λ_0	21.60 Å		18.97 Å		28.78 Å		24.78 Å		15.01 Å	
$f^{[a]}$	0.68		0.83		0.66		0.83		2.52	
	day 39.7	day 66.9	day 39.7	day 66.9	day 39.7	day 66.9	day 39.7	day 66.9	day 39.7	day 66.9
Absorption Component										
$^{[b]}v_s$	1143^{+939}_{-317}	-685^{+101}_{-104}	-1264^{+477}_{-254}	-772^{+91}_{-87}	-1365^{+907}_{-227}	–	-1098^{+444}_{-116}	-701^{+407}_{-78}	-1556^{+661}_{-426}	-834^{+439}_{-428}
$^{[c]}\tau_c$	$0.79^{+0.83}_{-0.46}$	$1.23^{+0.94}_{-0.45}$	$1.04^{+0.46}_{-0.85}$	$1.37^{+0.92}_{-0.44}$	$0.72^{+0.97}_{-0.40}$	< 3.0	$1.08^{+0.45}_{-0.40}$	$1.01^{+0.49}_{-0.24}$	$0.87^{+1.93}_{-0.87}$	$0.79^{+1.81}_{-0.60}$
$^{[d]}xn_0$	$3.38^{+1.04}_{-0.96}$	$3.17^{+0.61}_{-0.43}$	$4.53^{+0.59}_{-0.69}$	$4.53^{+0.44}_{-0.50}$	$1.88^{+0.47}_{-0.54}$	< 1.3	$3.25^{+0.35}_{-0.40}$	$2.42^{+0.24}_{-0.30}$	$1.23^{+0.81}_{-0.66}$	$1.25^{+0.54}_{-0.57}$
Emission Component										
$^{[b]}v_s$	633^{+316}_{-371}	–	544^{+402}_{-1334}	–	329^{+250}_{-1839}	–	559^{+593}_{-735}	3^{+583}_{-335}	363^{+383}_{-1969}	–
$^{[e]}\text{flux}$	$3.78^{+3.5}_{-2.0}$	–	$2.20^{+3.0}_{-0.9}$	–	31.9^{+18}_{-15}	–	$3.55^{+7.52}_{-2.56}$	$2.87^{+14}_{-2.9}$	$0.13^{+0.13}_{-0.05}$	–

$^{[a]}$ oscillator strength $^{[b]}$ velocity from line shift (km s⁻¹)

$^{[d]}$ column density (10¹⁶cm⁻²)

$^{[c]}$ optical depth at line center
 $^{[e]}$ emission line flux (10⁻¹⁰erg cm⁻²sec⁻¹)

$^{[d]}$ uncertainties of xn_0 were calculated at fixed wavelengths and with fixed emission line parameters and are underestimated

TABLE 3
STRONGEST ABSORPTION LINES FOUND IN OBSID 7296 (DAY 39.7)

$\lambda^{[a]}$	τ_c	$\lambda_0^{[a]}$	ID ^[b]	$\lambda^{[a]}$	τ_c	$\lambda_0^{[a]}$	ID ^[b]
14.93	0.86	15.01	Fe XVII	23.51	1.41	23.62	O I
15.77	0.41	15.87	Fe XVIII?	23.66	0.35	23.78	N VI
15.94	0.92	16.00	O VIII	24.50	0.24	24.51	S XIV?
16.71	0.43	16.78	Fe XVII	24.69	0.93	24.78	N VII
16.99	0.51	17.05	Fe XVII	25.61	0.57	25.68	Ar XVI?
17.69	0.48	17.77	O VII?	25.76	0.25	25.84	Ar XV?
18.88	1.00	18.97	O VIII	25.91	0.21	26.00	Ar XV?
19.84	0.75	19.83	N VII	26.07	0.51	26.12	N VI
20.63	0.43	20.68	S XIV?	26.82	1.06	26.99	C VI?
20.84	0.44	20.91	N VII	27.30	0.42	27.47	Ar XIV?
21.52	0.83	21.60	O VII	27.52	0.79	27.64	Ar XIV?
22.25	0.56	22.33	O V	27.83	0.49	27.90	Si XII?
22.64	1.18	22.78	O IV	28.00	0.55	28.11	Fe XX?
22.93	1.06	22.97	Ca XVI?	28.65	0.70	28.78	N VI
23.16	0.31	23.11	O III	29.80	0.66	29.91	Fe XVII?
	or	23.29	N VI	30.35	1.59	30.47	Ca XI?
23.36	0.25	23.30	O II	31.29	0.94	31.32	Fe XVIII?

$^{[a]}$ in Å

$^{[b]}$ Uncertain identifications are marked with '??'

originate from the shock, only interstellar absorption has to be accounted for, leading to line fluxes that suggest a mixture of collisional excitations and photoexcitations. Otherwise, circumstellar absorption has to be added, and stronger line fluxes would have to be assumed that could be explained by a smaller distance between the radiation source and the plasma emitting the soft lines.

3.4. He-like triplets

The most prominent transitions in the range 5 Å–45 Å are H-like and He-like lines of elements with nuclear charge $Z = 6$ (carbon) to $Z = 14$ (silicon). The $n = 2 - 1$ transitions of He-like ions consist of three strong lines, a resonance line (r: $1s2p^1P_1$) an intercombination line (i: $1s2p^3P_1$), and a forbidden line (f: $1s2s^3S_1$), all decaying into the ground state ($1s^2^1S_0$, see, e.g., Ness et al. 2003a). These lines are important for two reasons. First, the measured wavelengths of the intercombination- and forbidden lines can constrain the exact location of the emission line components in the models described in Sect. 3.2 because they are not absorbed. Second, the

flux ratio f/i of the He-like triplets are important density diagnostics (e.g., Gabriel & Jordan 1969; Ness et al. 2004). In low-density environments with the presence of strong UV fields, the f/i ratios can also be used to measure the distance between the X-ray plasma and the UV source (applied, e.g., by Waldron & Cassinelli 2001, to the winds of O stars immersed in the UV radiation field from the stellar surface).

We used our line fitting tool Cora (Ness & Wichmann 2002) to determine the line positions and line fluxes of the He-like lines of O VII, $\lambda_0 = (21.6, 21.8, 22.1)$ Å, and N VI $\lambda_0 = (28.78, 29.1, 29.54)$ Å, using Gaussian line profiles. We varied the line positions and found that the i and f lines are not significantly shifted from their rest wavelengths (upper limit ~ 600 km s⁻¹). More refined models in Sect. 3.2 can therefore be calculated with the boundary condition that the emission line components are not shifted.

Next, we measured the line fluxes with variable line strengths and fixed wavelengths and line widths on top of a constant continuum. For O VII we used a constant value of 9000 counts per Å and for N VI where the continuum is not as flat as for O VII, we used a linear continuum with a slope of -40 counts per Å. In Fig. 7 we show the spectra and our models for day 39.7.

We considered the possibility that the lines shortwards of the forbidden lines (~ 22 Å and ~ 29.4 Å) are blue-shifted counterparts of the forbidden lines. In that case the intercombination lines should also have blue-shifted companions at the same velocity. For O VII a model with an additional component, shifted by -1763.5 km s⁻¹, results in a good representation of the data (top panel of Fig. 7). For N VI the forbidden line clearly shows a second component at a different velocity, but there is no evidence for a blue-shifted component of the intercombination line at this velocity. No transitions from other ions are known for these wavelengths that would be strong enough, but these lines could be satellite lines that appear in a photoionized recombining plasma. For our further analysis we only use the fluxes measured at the rest wavelengths.

We include the measured fluxes for the i- and f lines in Table 4. In a collisional plasma the sum of the fluxes in the i- and f- lines is expected to be of the same order as that in the resonance line (r), while in a plasma where

TABLE 4
EVOLUTION OF EMISSION LINE FLUXES.

Ion	$\lambda_0^{[a]}$ (Å)	TC ^[b1]	TC ^[b2]	flux ^[c]			ratio		
				day 39.6	day 54.0	66.9	54/39	66/54	66/39
Lines from shock ('hard lines')									
Si XIV	6.18	0.841	0.897	112.1 ± 10.6	47.2 ± 12.8	22.1 ± 6.3	0.42	0.47	0.20
Si XIII	6.65	0.809	0.876	336.4 ± 55.5	158.3 ± 68.2	50.9 ± 33.1	0.47	0.32	0.15
Mg XII	8.42	0.693	0.793	196.8 ± 12.3	106.7 ± 7.9	40.5 ± 7.2	0.54	0.38	0.21
Mg XI	9.20	0.626	0.744	386.3 ± 38.1	240.2 ± 26.5	133.3 ± 27.7	0.62	0.56	0.35
Ne X	12.13	0.390	0.556	285.5 ± 11.8	105.7 ± 9.3	95.2 ± 8.3	0.37	0.90	0.33
Fe XVII	12.26	0.380	0.547	70.2 ± 11.5	17.4 ± 8.1	26.5 ± 8.6	0.25	1.52	0.38
Ne IX	13.44	0.290	0.463	138.1 ± 13.8	42.0 ± 5.5	34.1 ± 11.4	0.30	0.81	0.25
Ne IX ^[i]	13.55	0.282	0.455	66.7 ± 8.0	28.8 ± 4.1	38.1 ± 8.1	0.43	1.32	0.57
Ne IX ^[i]	13.69	0.273	0.445	104.4 ± 9.9	36.4 ± 3.8	52.5 ± 8.4	0.35	1.45	0.50
Fe XVIII	14.20	0.239	0.410	48.7 ± 6.6	–	20.7 ± 9.1			0.42
Lines on top of the SSS spectrum ('soft lines')									
Fe XVII	15.01	0.225	0.403	170 ⁺¹⁷⁰ ₋₇₀	–	–			
O VIII	18.97	0.087	0.226	848 ⁺¹¹⁴⁰ ₋₁₃₀	–	–			
O VII	21.60	0.031	0.121	361 ⁺³⁴⁰ ₋₁₉₀	–	–			
O VII ^[i]	21.80	0.028	0.115	381.8 ± 24.6	–	–			
O VII ^[i]	22.10	0.025	0.106	418.2 ± 24.6	–	–			
N VII	24.78	0.051	0.181	400 ⁺⁸⁵⁰ ₋₂₉₀	–	321 ⁺¹³⁸⁰ ₋₃₂₀			
N VI	28.78	0.010	0.072	325 ⁺¹⁸⁰ ₋₁₅₀	–	247 ⁺⁹²⁰ ₋₂₅₀			
N VI ^[i]	29.10	0.009	0.066	282.1 ± 19.1	–	443.9 ± 31.9			
N VI ^[i]	29.54	0.007	0.059	788.5 ± 27.3	–	397.7 ± 32.6			

^[a]rest wavelengths ^{[b1],[b2]}transmission coefficients assuming ^[b1]N_H = 4.7 × 10²¹ cm⁻² and ^[b2]2.4 × 10²¹ cm⁻²
^[c]10⁻¹⁴ erg cm⁻² s⁻¹, not corrected for interstellar absorption ^[i]intersystem line

photoexcitation takes place, the ratio $G = (f+i)/r$ should be less than 1. If this ratio is greater than one, this indicates a purely recombining plasma or a photoionized plasma with high column densities suppressing resonant diffusion (Coupé et al. 2004; Godet et al. 2004). From the numbers in Table 4 we compute $G = 2.2 \pm 1.2$ for O VII and $G = 3.3 \pm 2.0$ for N VI, both greater than one, but with large uncertainties.

At low densities the ratio of $R = f/i$ is expected to be 3.9 for O VII and 4.9 for N VI (low-density limit R_0), while in a high-density plasma, this ratio is reduced by collisional excitations from the upper level of the f-line into the upper level of the i-line, followed by radiative de-excitations from there into the ground. We measured f/i ratios of 1.1 ± 0.1 and 2.8 ± 0.2 , which correspond to densities of $\log(n_e) = 11$ and $\log(n_e) = 10.8$ for O VII and N VI, respectively. We used the summarized parameterized form given by, e.g., equation 2 in Ness et al. (2004) that has been derived by Gabriel & Jordan (1969) with the critical densities $\log(N_c) = 10.5$ and $\log(N_c) = 9.7$ for O VII and N VI, respectively. As a first approach, we neglected the radiation term ϕ/ϕ_c . For comparison, Evans et al. (2007) measured densities of order $10^5 - 10^{10}$ cm⁻³ from various infrared lines between days 64 and 84, and our values are rather high compared to that. However, the IR and the X-ray emission may originate from different places in the flow, especially if the X-ray lines originate from the shock (see previous section).

We next study the possibility that UV radiation fields lead to the low f/i ratios. Ness et al. (2003a) have given a method that converts measured UV fluxes at the wavelengths ~ 1630 Å for O VII and at ~ 1900 Å for N VI into the parameter ϕ/ϕ_c that we have neglected above (see also Blumenthal et al. 1972; Waldron & Cassinelli 2001). This method includes a dilution factor which

can be converted into the distance between the plasma and the UV radiation source, assuming a distance to RS Oph of 1.6 kpc. We examined the simultaneous UVOT Grism data taken with *Swift*, but the data are not calibrated yet, and the wavelength range around 1630 Å is not covered. We, therefore, inspected the archive of the International Ultraviolet Explorer satellite (IUE), which contains a number of observations of RS Oph taken after the outburst on 1985, January 28 (e.g. Shore et al. 1996). We extracted an observation taken 1985, Feb. 26, 23:47:00UT (~ 30 days after outburst; ObsID SWP25327) and estimated flux levels for the continuum of $\sim 2 \times 10^{-13}$ erg cm⁻² sec⁻¹ at 1630 Å and 1900 Å. Emission lines near these wavelengths from He II (1640 Å), Si III] (1892 Å), and C III] (1908 Å; Shore et al. 1996) can increase the relevant flux to no more than 10^{-12} erg cm⁻² sec⁻¹. The former flux level leads to a distance between the UV source and the immersed plasma of $\sim 4 \times 10^{11}$ cm ($6 R_\odot$) for O VII and $\sim 3 \times 10^{12}$ cm ($40 R_\odot$) for N VI, while the latter flux leads to $\sim 9 \times 10^{11}$ cm ($13 R_\odot$) and $\sim 10^{13}$ cm ($180 R_\odot$) for O VII and N VI, respectively. These numbers are quite uncertain because we assume that the UV emission level was similar during the 1985 and 2006 outbursts. However, we can conclude that if the plasma emitting these lines is further away from the UV radiation source, than $200 R_\odot$, then the density must be higher than 10^{10} cm⁻³. This distance is small compared to the extent of the expanding shell on day 39.7. With an expansion velocity of 1100 km s⁻¹ the shell has reached a radius of 3.8×10^{14} cm ($5400 R_\odot$).

3.5. Spectral Variability from High- to Low-flux phases

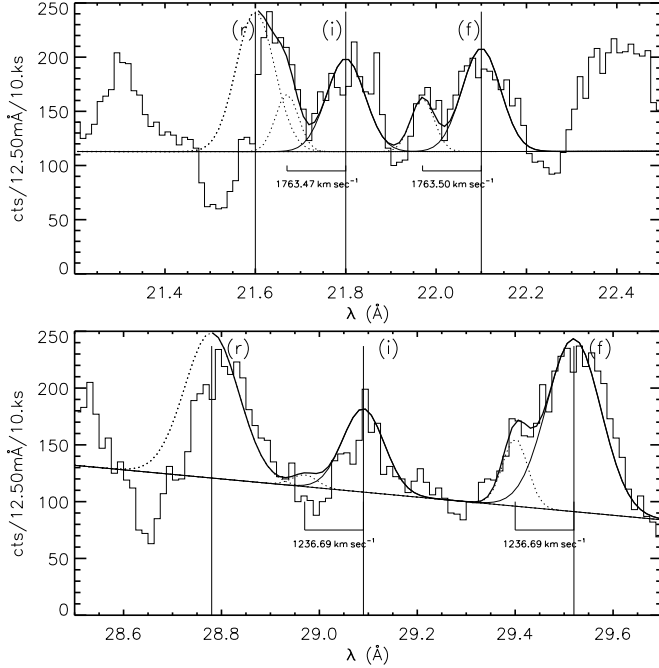


FIG. 7.— Spectral region around the He-like triplets of O VII (top) and N VI (bottom) on day 39.7. The respective resonance lines (r) at 21.6 and 28.78 Å are seen in absorption and emission while, the intercombination- (i) and forbidden (f) lines are only seen in emission, giving us the likely wavelengths of all emission lines. Gaussian fits to the lines reveal no line shifts (upper limit $\sim 600 \text{ km s}^{-1}$). Additional lines are seen shortwards of the forbidden lines, that could come from a velocity component with -1763 km s^{-1} and -1237 km s^{-1} for O VII and N VI, respectively, but no counterpart in the N VI intercombination line is detected.

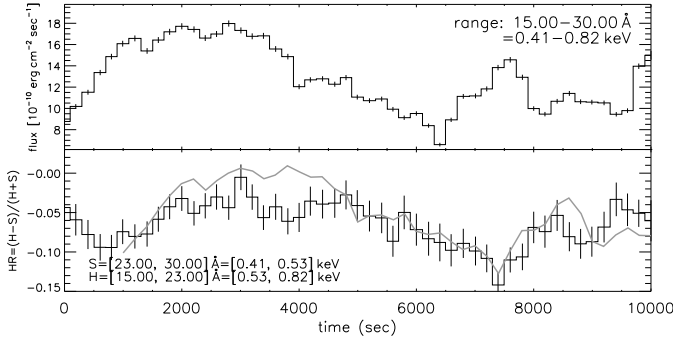


FIG. 8.— **Top:** *Chandra* light curve extracted from the dispersed photons in the wavelength range 15–30 Å (day 39.7). **Bottom:** evolution of hardness ratio (in steps of 200 sec) defined by the energy ranges given in the legend. The grey curve is the light curve from the top panel, shifted by 1000 sec on the time axis and rescaled with a factor 0.012.

We now focus on spectral changes on shorter time scales. During the observation taken on day 39.7, variations in brightness were detected which were not seen in the other two observations. In Fig. 8 we show the evolution of the observed flux integrated over the wavelength range 15–30 Å (top panel) in comparison to the hardness ratio HR (bottom panel) with the same definitions as used in Sect. 2.2 (repeated in the legend). The rescaled light curve, marked with the grey curve in the bottom panel of Fig. 8 indicates that the hardness ratio has the same shape but is retarded by 1000 sec.

In order to study the spectral changes in more detail, we extracted spectra from the two different time intervals

marked in dark and light shadings in Fig. 1, representing high-flux and low-flux emission. In Fig. 9 we compare these spectra with the dark shading being the high-flux spectrum and the light shading the low-flux spectrum. In the bottom two panels we show the cumulative distribution of counts and the ratio spectrum, respectively.

The cumulative distribution traces the spectral shape regardless of the different intensities and can be used for a Kolmogorov-Smirnov 2-sample test. At $\sim 27 \text{ Å}$ we find the largest difference of 0.03, which has to be compared to the maximally allowed difference of 0.007 if the two spectra were to be considered identical within 95 percent probability. The spectra are therefore different in their shapes in addition to the obvious difference of intensity. Inspection of the cumulative curve reveals that the high-flux spectrum is slightly softer.

The ratio spectrum shows up to a factor of two higher emission in the high-flux spectrum. The absorption lines of O VIII at 19 Å and N VII at 25 Å as well as the O I absorption edge at 22.83 Å are deeper relative to the continuum in the high-flux spectrum. This indicates that the brightness changes involve more than changes in the brightness of the continuum. In contrast, shortwards of 15 Å as well as near 29.5 Å (the wavelength of the N VI forbidden line) the two spectra are identical.

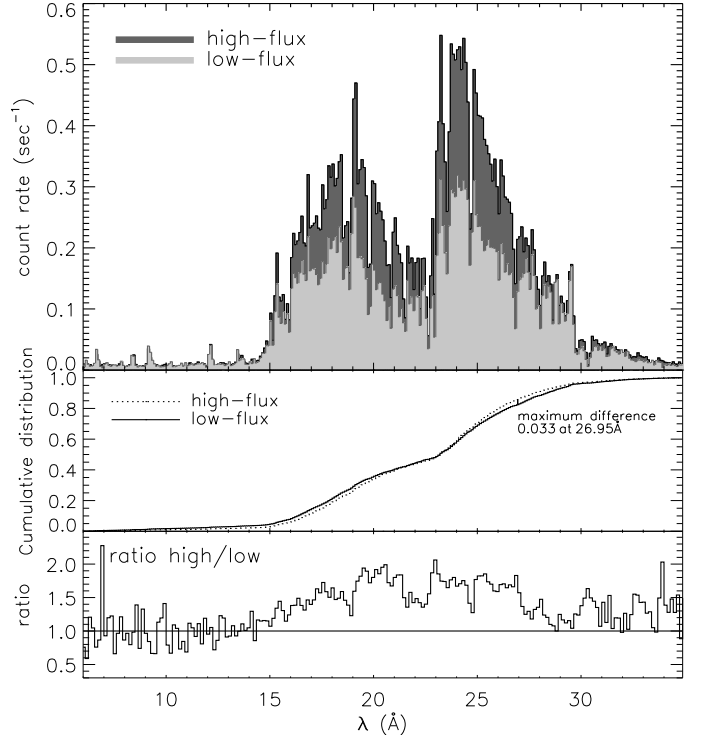


FIG. 9.— Comparison of spectra extracted from high-flux and low-flux intervals in ObsID 7296. **Top:** direct comparison of count rate spectra. **Middle:** Cumulative count distribution. **Bottom:** Ratio of spectra.

In Fig. 10 we compare the high-flux and low-flux spectra around the absorption lines in velocity space. While the high-flux phase provides additional continuum emission, the emission level in the troughs of the absorption lines is unchanged. There is no detectable difference in blue shift of the absorption troughs.

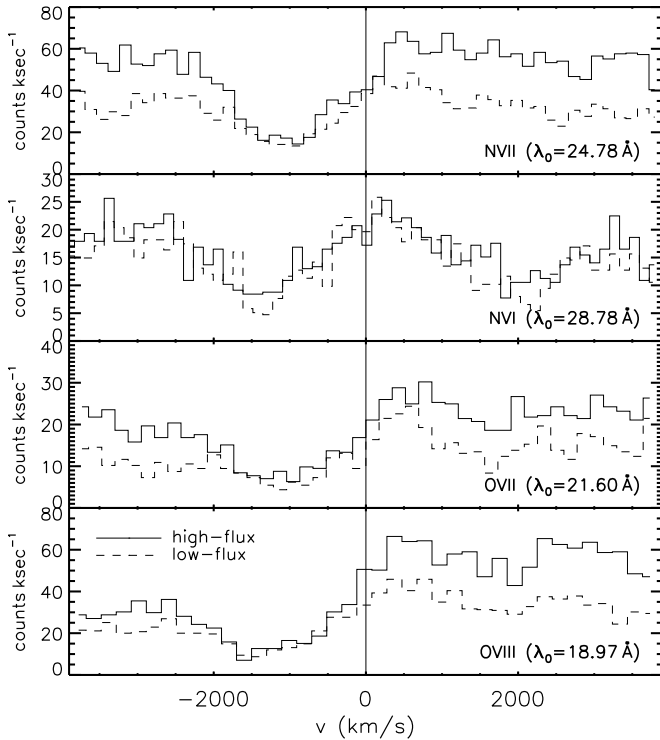


FIG. 10.— Details of *Chandra* spectra of day 39.7 for high-flux (solid) and low-flux (dashed) phases, plotted in velocity space for the lines indicated in the legends of each panel. The absorption lines are blue shifted by the same amount in both spectra.

We repeated our model from Sect. 3.2 for these two spectra. While the optical depths at line center were around unity for both spectra, the line column densities were significantly lower in the low-flux observation. For example, for O VIII we found a column density of $6.33^{+1.58}_{-1.51}$ in the high-flux spectrum but only $2.93^{+1.92}_{-1.16}$ in the low-flux spectrum. The line shift velocities were the same in the models to both spectra.

4. DISCUSSION

In Sect. 3 we have presented a number of issues that can be addressed with the three grating spectra of RS Oph. The shape of the spectrum cannot be approximated by a blackbody model. The dominant feature, the O I absorption edge, changes with time. The quantitative analysis of these changes is complicated by various overlapping absorption processes. For example, the ionization edges and 1s-2p transitions from oxygen in low ionization stages introduce significant structure to the observed spectrum. These low ionization stages can occur in both the circumstellar and the interstellar material in the line of sight. We thus need a more refined model accounting for more processes than only K-shell ionization of neutral elements in order to understand the effects that the interstellar plus circumstellar material have on the observed spectra.

These uncertainties affect the interpretation of the origin and production mechanism of the soft emission lines listed in the bottom part of Table 4. While the hard lines at short wavelengths can only be collisionally excited and originate from the shock, the soft lines can in addition be photoexcited because of the presence of the bright SSS spectrum. The contribution from photoexcitations depends on the distance between the hot WD

atmosphere that provides the radiation and the plasma that emits the soft lines. If they originate from the shock, this distance will be greater than if they are part of the hot WD atmosphere. In the latter case the soft lines should be much stronger than in the former case. However, the amount of assumed extinction will be enhanced by circumstellar material in addition to the interstellar medium, leading to lower line fluxes measured at Earth. In order to solve the ambiguity from these competing processes, an improved absorption model for interstellar and circumstellar absorption is required to derive accurate unabsorbed lines fluxes for each case. The hard lines can be used to constrain the mean emission measure distribution for a collisional plasma as developed by Ness et al. (2005) for the Classical Nova V382 Vel. This will be part of an upcoming paper (Ness et al. in prep). If the soft lines originate from the shock, they will show up with an excess in the emission measure distribution, reflecting the contributions from photoexcitations. The amount of excess depends on the distance between the plasma and the hot WD atmosphere, which has to be of the same order as that between atmosphere and the shocked plasma. We note that the disappearance of the soft emission lines between days 39.7 and 66.9 is consistent with the fading of the lines produced in the shock. The only soft lines measurable on day 66.9 were also weaker than on day 39.7, even though the SSS spectrum was brighter. We thus favor a scenario in which the soft lines originate from the shock and are partially photoexcited, while being absorbed only by interstellar material.

The optical depths at line center and the velocities derived from the absorption lines (Sect. 3.2) are not affected by the uncertainties in interstellar and/or circumstellar absorption. The reduction of the velocities is due to observing deeper into the flow at the time of the later observation.

Our absorption line model can be improved beyond the results presented in Table 2. First, we need to include the instrumental line profile in order to explore the line widths. From our conclusion in Sect. 3.4 we can define the boundary condition that the emission line components are at their rest wavelengths, which leads to a reduction of the uncertainties of the other parameters. Our above conclusion that the soft emission lines likely originate from the shock has to be accounted for by not allowing self absorption. We repeated our models without self absorption and found similar results, such that our results are robust.

The issue of the appearance of P Cygni type profiles on day 39.7 cannot fully be answered at this stage. The shape of the absorption lines is not typical for P Cygni profiles, which usually show a sharp blue edge which represents the terminal velocity of the wind. Our finding of symmetric absorption lines indicates that we are not observing the entire velocity profile but only a fraction of it. Those plasma regions that reside at the terminal velocity (in velocity space) could be optically thin and thus contribute little to the absorption lines. In the same way, this plasma may also be too thin to produce measurable emission lines, that would be scattered into our direction from the photoexcited plasma moving perpendicularly to the line of sight, further supporting our above conclusion that the soft lines originate from the shock. Also, the He-like resonance lines are expected to be significantly

stronger than the intersystem lines if photoexcitation of the circumstellar material was dominant.

The high degree of variability during the first week of the SSS phase (including our observation on day 39.7) is a new discovery that has not been observed in any other nova. However, we have never had the same frequency of observations of the same event. In one case, V4743 Sgr (Ness et al. 2003b), a decline of X-ray brightness occurred, which may be a similar phenomenon. Although this decay is only seen during the first of four observations taken during the SSS phase, it is not known when the SSS phase started, and thus how early in the SSS evolution the decline was observed. Variability was also observed in V1494 Aql, V4743 Sgr, and V832 Vel, but the amplitude was much lower and the variations were periodic (e.g., Ness et al. 2003b; Drake et al. 2003).

In our *Chandra* observation on day 39.7 we discovered the hardness ratio light curve lagging behind the total light curve by 1000 s. The hardness ratio is commonly used as a temperature indicator. If the temperature varies, then this leads to an increase in brightness before the spectral hardness increases. Temperature variations could occur periodically, but we did not detect any periods in the observation on day 39.7. With the existing observations, we cannot exclude the presence of any periods longer than three hours or shorter than a few days. However, photoionization of oxygen could also lead to the higher hardness ratios, as ionized oxygen allows more hard emission to pass through. In this case the material in the line of sight responds to the brightness of the continuum emission by adjusting the degree of ionization within 1000 s. This timescale would be the same for ionization and recombination and implies a density of the absorbing material of $\sim 10^{10} - 10^{11} \text{ cm}^{-3}$. This is consistent with the densities derived from the He-like triplets, and the changes in hardness can therefore be explained by variations in the degree of ionization of the circumstellar material. However, this does not explain the origin of the brightness changes.

The spectra extracted from two different time intervals during the episode of high-amplitude variations show complex changes. We found deeper absorption lines and a deeper oxygen edge during times of brighter continuum emission. This shows that the brightness variations are correlated to the absorption behavior of the expanding shell and the surrounding material and each spectrum must be treated independently.

As an example, we applied our model from Sect. 3.2 to the two spectra presented in Sect. 3.5 and found higher column densities during the high-flux phase while the velocities were the same for both spectra. Higher column densities arise when we either look deeper into the outflow (longer path length) or when the density is higher (or both). The high-flux phases can have their origin in a reduction of the opacity, allowing us to view deeper into the outflow where more emission is produced, the densities are higher, and the temperatures are higher.

Most of our results are based on preliminary models, and we are improving these models. The first steps will have to improve the atmosphere and the model for interstellar and circumstellar absorption. The stellar atmosphere has to be modeled as an expanding atmosphere with PHOENIX (e.g. Petz et al. 2005). The O edge has not been explored much, and new models have to be de-

veloped (see, e.g., Paerels et al. 2001). We will further improve our model that fits the absorption and emission lines simultaneously (Schönrich et al. in prep). With improved models in place, the changes of temperatures, luminosities and absorption behavior during the phase of extreme variability can be determined. A separate analysis of the emission lines and continuum produced in the shocked plasma is under way (Ness et al. in prep), and more detailed hydrodynamic models are being developed for comparison with the data (see e.g. Vaytet et al. 2007). Finally, the *Swift* spectra can be used to constrain the evolution between the grating observations. The model parameters obtained from grating spectra on days 37.9, 54.0, and 66.9 can be interpolated for days on which *Swift* spectra are available. The spectral models obtained from the interpolated parameters have to agree with the respective measured *Swift* spectra.

5. SUMMARY AND CONCLUSIONS

The X-ray grating spectra of the SSS phase are complex and contain a great deal of information. The objective of this paper is to provide an overview of the physical information that can be obtained from X-ray data. We have found:

- The brightness changes between the three observations are consistent with the variations measured from the *Swift* observations at the same epochs.
- Short-period oscillations (~ 35 sec), first detected in some of the *Swift* observations, are confirmed. We discovered that this period resides in the plasma that emits the SSS spectrum.
- The episode of high-amplitude variations detected with *Swift* that occurs on time scales of days is accompanied by variations on time scales of hours.
- The depth of the O I absorption edge is variable, yielding the lowest optical depth on day 54.0. One possible explanation is photoionization of the absorbing material in the line of sight.
- The absorption lines are shifted by $-1286 \pm 267 \text{ km s}^{-1}$ on day 39.7 and $-771 \pm 65 \text{ km s}^{-1}$ on day 66.9.
- Declining emission from the shock is observed in the form of collisionally excited emission lines shortwards of the SSS continuum. These lines are slightly blue-shifted.
- Superimposed on the SSS spectrum are emission lines whose origin could either be from the shocked plasma or from photoexcited material in the outer regions of the outflow.
- Intersystem lines from He-like ions, are found at their rest wavelengths. The ratio (i+f)/r (r the 1s-2p resonance line) is greater than one, indicating contributions from recombination into excited states and small contributions from resonance scattering. The ratio f/i indicates either densities in excess of 10^{11} cm^{-3} or a short distance between the plasma containing the He-like ions and a source for UV radiation.

- The brightness changes during the phase of variability induce changes in spectral hardness, retarded by 1000 sec. Absorption lines and the O edge are deeper during high-state phases, and if the density of the absorbing material is of order $10^{10} - 10^{11} \text{ cm}^{-3}$, then the hardness changes can exclusively be explained by ionization. In that case the increases and reduction of brightness occur underneath the absorbing material, possibly in the regions where nuclear burning takes place.

JUN gratefully acknowledges support provided by NASA through *Chandra* Postdoctoral Fellowship grant PF5-60039 awarded by the *Chandra* X-ray Center, which is operated by the Smithsonian Astrophysical Observatory for NASA under contract NAS8-03060. SS received partial support from NSF and NASA grants to ASU. PHH was supported in part by DFG grant HA 3457/2 and by the Pôle Scientifique de Modélisation Numérique at ENS-Lyon. KLP, JPO, APB, and MRG acknowl-

edge support by the Particle Physics and Astronomy Research Council. MFB is grateful to the UK PPARC for the provision of a Senior Fellowship. RS acknowledges support from Stiftung Maximilianeum, Studienstiftung des deutschen Volkes, and the Max-Weber-Programm. We are grateful to Harvey Tananbaum and the *Chandra* Observatory for a generous allotment of Directors Discretionary. Some of the observations have been obtained with XMM-Newton, an ESA science mission with instruments and contributions directly funded by ESA Member States and NASA. Some preliminary calculations carried out for this project were performed at the Höchstleistungs Rechenzentrum Nord (HLRN), and at the National Energy Research Supercomputer Center (NERSC), supported by the U.S. DOE, and at the computer clusters of the Hamburger Sternwarte, supported by the DFG and the State of Hamburg. We thank all these institutions for a generous allocation of computer time. We thank an anonymous referee for instructive comments.

REFERENCES

- Blumenthal, G. R., Drake, G. W. F., & Tucker, W. H. 1972, *ApJ*, 172, 205
- Bode, M. F. 1987, in RS Ophiuchi (1985) and the Recurrent Nova Phenomenon, ed. M. F. Bode, 241
- Bode, M. F., Harman, D., O'Brien, T. J., Bond, H. E., Starrfield, S., Darnley, M. J., Eyres, S., & Evans, A. 2007, submitted to *ApJL*
- Bode, M. F., O'Brien, T. J., Osborne, J. P., Page, K. L., Senziani, F., Skinner, G. K., Starrfield, S., Ness, J.-U., Drake, J. J., Schwarz, G., Beardmore, A. P., Darnley, M. J., Eyres, S. P. S., Evans, A., Gehrels, N., Goad, M. R., Jean, P., Krautter, J., & Novara, G. 2006, *ApJ*, 652, 629
- Brinkman, B. C., Gusing, T., Kaastra, J. S., van der Meer, R., Mewe, R., Paerels, F. B., Raassen, T., van Rooijen, J., Braeuninger, H. W., Burwitz, V., Hartner, G. D., Kettenring, G., Predehl, P., Drake, J. J., Johnson, C. O., Kenter, A. T., Kraft, R. P., Murray, S. S., Ratzlaff, P. W., & Wargelin, B. J. 2000, *SPIE*, 4012, 81
- Chesneau, O., Nardetto, N., Millour, F., Hummel, C., Domiciano de Souza, A., Bonneau, D., Vannier, M., Rantakyro, F., Spang, A., Malbet, F., Mourard, D., Bode, M. F., O'Brien, T. J., Skinner, G., Petrov, R. G., Stee, P., Tatulli, E., & Vakili, F. 2007, *A&A*, 464, 119
- Coupé, S., Godet, O., Dumont, A.-M., & Collin, S. 2004, *A&A*, 414, 979
- den Herder, J. W., Brinkman, A. C., Kahn, S. M., Branduardi-Raymont, G., Thomsen, K., Aarts, H., Audard, M., Bixler, J. V., den Boggende, A. J., Cottam, J., Decker, T., Dubbeldam, L., Erd, C., Goulooze, H., Güdel, M., Guttridge, P., Hailey, C. J., Janabi, K. A., Kaastra, J. S., de Korte, P. A. J., van Leeuwen, B. J., Mauche, C., McCalden, A. J., Mewe, R., Naber, A., Paerels, F. B., Peterson, J. R., Rasmussen, A. P., Rees, K., Sakellidou, I., Sako, M., Spodek, J., Stern, M., Tamura, T., Tandy, J., de Vries, C. P., Welch, S., & Zehnder, A. 2001, *A&A*, 365, L7
- Dobrzycka, D., & Kenyon, S. J. 1994, *AJ*, 108, 2259
- Drake, J. J., Ness, J. U., & Starrfield, S. 2006, *ApJL* in prep
- Drake, J. J., Wagner, R. M., Starrfield, S., Butt, Y., Krautter, J., Bond, H. E., Della Valle, M., Gehr, R. D., Woodward, C. E., Evans, A., Orio, M., Hauschildt, P., Hernanz, M., Mukai, K., & Truran, J. W. 2003, *ApJ*, 584, 448
- Evans, A., Woodward, C., Helton, A., Gehr, R. D., Lynch, D. K., Rudy, R. J., Russell, R. W., Kerr, T., & al. 2007, submitted to *MNRAS*
- Gabriel, A. H., & Jordan, C. 1969, *MNRAS*, 145, 241
- Gallagher, J. S., & Code, A. D. 1974, *ApJ*, 189, 303
- Godet, O., Collin, S., & Dumont, A.-M. 2004, *A&A*, 426, 767
- Gonzalez-Riestra, R., Orio, M., & Leibowitz, E. 2006, *IAU Circular*, 8695, 2
- Grevesse, N., & Sauval, A. J. 1998, *Space Science Reviews*, 85, 161
- Hirosawa, K., Narumi, H., Kanai, K., & Renz, W. 2006, *Central Bureau Electronic Telegrams*, 399, 1 (2006). Edited by Green, D. W. E., 399, 1
- Hjellming, R. M., van Gorkom, J. H., Seaquist, E. R., Taylor, A. R., Padin, S., Davis, R. J., & Bode, M. F. 1986, *ApJL*, 305, L71
- Jansen, F., Lumb, D., Altieri, B., Clavel, J., Ehle, M., Erd, C., Gabriel, C., Guainazzi, M., Gondoin, P., Much, R., Munoz, R., Santos, M., Schartel, N., Texier, D., & Vacanti, G. 2001, *A&A*, 365, L1
- Juett, A. M., Schulz, N. S., & Chakrabarty, D. 2004, *ApJ*, 612, 308
- Kahabka, P., & van den Heuvel, E. P. J. 1997, *ARA&A*, 35, 69
- Kashyap, V., & Drake, J. J. 2000, *Bulletin of the Astronomical Society of India*, 28, 475
- Mason, K. O., Córdova, F. A., Bode, M. F., & Barr, P. 1987, in RS Ophiuchi (1985) and the Recurrent Nova Phenomenon, 167
- Murray, S. S., Austin, G. K., Chappell, J. H., Gomes, J. J., Kenter, A. T., Kraft, R. P., Meehan, G. R., Zombeck, M. V., Fraser, G. W., & Serio, S. 2000, *SPIE*, 4012, 68
- Ness, J.-U., Güdel, M., Schmitt, J. H. M. M., Audard, M., & Telleschi, A. 2004, *A&A*, 427, 667
- Ness, J.-U., Mewe, R., Schmitt, J. H. M. M., & Raassen, A. J. J. 2003a, in *The Future of Cool-Star Astrophysics: 12th Cambridge Workshop on Cool Stars, Stellar Systems, and the Sun (2001 July 30 - August 3)*, 2003, ed. A. Brown, G.M. Harper, and T.R. Ayres (University of Colorado), 265-274
- Ness, J.-U., Starrfield, S., Burwitz, V., Wichmann, R., Hauschildt, P., Drake, J. J., Wagner, R. M., Bond, H. E., Krautter, J., Orio, M., Hernanz, M., Gehr, R. D., Woodward, C. E., Butt, Y., Mukai, K., Balman, S., & Truran, J. W. 2003b, *ApJL*, 594, L127
- Ness, J.-U., Starrfield, S., Drake, J. J., Orio, M., Bode, M. F., O'Brien, T. J., Davis, R. J., Osborne, J., Page, K. L., Schwarz, G., Krautter, J., Evans, A., Eyres, S. P. S., Gehr, R., & Woodward, C. 2006a, *IAUC*, 8683, 2
- Ness, J.-U., Starrfield, S., Drake, J. J., Orio, M., Gonzalez-Riestra, R., Bode, M. F., O'Brien, T. J., Davis, R. J., Osborne, J. P., Page, K. L., Beardmore, A., Goad, M., Schwarz, G., Krautter, J., Evans, A., Eyres, S. P. S., Gehr, R., Woodward, C., & Gehrels, N. A. 2006b, *Central Bureau Electronic Telegrams*, 498, 1 (2006). Edited by Green, D. W. E., 498, 1

- Ness, J.-U., Starrfield, S., Jordan, C., Krautter, J., & Schmitt, J. H. M. M. 2005, *MNRAS*, 364, 1015
- Ness, J.-U., Starrfield, S., Page, K., Osborne, J., Beardmore, A., & Drake, J. 2007, in *Progress of Theoretical Physics*, Supplement, in press
- Ness, J.-U., & Wichmann, R. 2002, *Astronomische Nachrichten*, 323, 129
- O'Brien, T. J., Bode, M. F., & Kahn, F. D. 1992, *MNRAS*, 255, 683
- O'Brien, T. J., Bode, M. F., Porcas, R. W., Muxlow, T. W. B., Eyres, S. P. S., Beswick, R. J., Garrington, S. T., Davis, R. J., & Evans, A. 2006, *Nature*, 442, 279
- Osborne, J., Page, K., Beardmore, A., Bode, M., O'Brien, T., Schwarz, G., Starrfield, S., Ness, J.-U., Krautter, J., Drake, J., Evans, A., & Eyres, S. P. S. 2006a, *The Astronomer's Telegram*, 764, 1
- Osborne, J., Page, K., Goad, A. B. M., Bode, M., O'Brien, T., Schwarz, G., Starrfield, S., Ness, J.-U., Krautter, J., Drake, J., Evans, A., & Eyres, S. P. S. 2006b, *The Astronomer's Telegram*, 801, 1
- . 2006c, *The Astronomer's Telegram*, 770, 1
- Osborne, J. P., Page, K. L., Beardmore, A. P., Goad, M. R., Bode, M. F., O'Brien, T. J., Starrfield, S., Ness, J.-U., Krautter, J., Schwarz, G., Burrows, D. N., Gehrels, N., Drake, J. J., & Eyres, S. P. S. 2007, in prep for *ApJ*
- Padin, S., Davis, R. J., & Bode, M. F. 1985, *Nature*, 315, 306
- Paerels, F., Brinkman, A. C., van der Meer, R. L. J., Kaastra, J. S., Kuulkers, E., den Boggende, A. J. F., Predehl, P., Drake, J. J., Kahn, S. M., Savin, D. W., & McLaughlin, B. M. 2001, *ApJ*, 546, 338
- Page, M. J., Soria, R., Wu, K., Mason, K. O., Cordova, F. A., & Priedhorsky, W. C. 2003, *MNRAS*, 345, 639
- Petz, A., Hauschildt, P. H., Ness, J.-U., & Starrfield, S. 2005, *A&A*, 431, 321
- Shore, S. N., Kenyon, S. J., Starrfield, S., & Sonneborn, G. 1996, *ApJ*, 456, 717
- Smith, R. K., Brickhouse, N. S., Liedahl, D. A., & Raymond, J. C. 2001, *ApJL*, 556, L91
- Snijders, M. A. J. 1987, in *RS Ophiuchi (1985) and the Recurrent Nova Phenomenon*, ed. M. F. Bode, 51
- Sokoloski, J. L., Luna, G. J. M., Mukai, K., & Kenyon, S. J. 2006, *Nature*, 442, 276
- Vaytet, N. M. H., O'Brien, T. J., & Bode, M. F. 2007, *ArXiv e-prints*, 704
- Waldron, W. L., & Cassinelli, J. P. 2001, *ApJL*, 548, L45
- Weisskopf, M. C., Brinkman, B., Canizares, C., Garmire, G., Murray, S., & Van Speybroeck, L. P. 2002, *PASP*, 114, 1